Journal of Fluids and Structures 143 (2026) 104538

Contents lists available at ScienceDirect

Journal of Fluids and Structures

journal homepage: www.elsevier.com/locate/jfs

From vortex shedding to Vortex-Induced Vibrations: The role of porous façades

Marcello Catania [1,*], Giulia Pomaranzi, Alberto Zasso

Dept. Mechanical Engineering, Politecnico di Milano, via G. La Masa 34, Milano, 20156, Italy

ARTICLE INFO

Keywords:
Porous facade
Permeable coverings
Vortex shedding
Vortex-Induced vibrations
Wind tunnel testing
Large-Eddy simulation
Darcy-forchheimer model

ABSTRACT

This work examines the aerodynamic and aeroelastic effects of a porous envelope applied to a rectangular prism with aspect ratio $B/D = 3.33$, representative of a high-rise building. Wind tunnel tests on rigid and aeroelastic models were combined with Large-Eddy Simulations (LES) using a Darcy-Forchheimer homogenized representation of porosity. On the rigid model, the porous shroud alters vortex shedding by introducing new separation points, widening the wake, and shifting the dominant Strouhal number to lower values. The numerical model reproduces these effects with good accuracy, confirming the suitability of the homogenized approach for capturing porosity-induced modifications. Aeroelastic tests reveal that the porous façade can suppress VIV initiation by disrupting force coherence during the first oscillation cycles, while external perturbations restore synchronization and lead to full VIV development. The results demonstrate that the mitigation effect of porosity is conditional and state-dependent, providing new insight into its potential as a VIV control strategy for civil structures.

1. Introduction

Vortex shedding (VS) is the phenomenon where alternating periodic vortices are shed from a bluff body in a fluid flow, creating oscillating lift forces. Vortex-induced vibration (VIV) occurs when the vortex shedding frequency matches the natural frequency of the oscillating structure, leading to resonant, amplified vibrations. Slender structures, such as long-span bridges, towers, and high-rise buildings, are particularly vulnerable to VIV, facing risks ranging from serviceability issues to fatigue damage (Li et al., 2016; Wang et al., 2024).

The rectangular cylinder is often adopted as a simplified model to study the aerodynamics of civil structures. Being the shedding frequency directly affected by the interaction between the fluid flow and the body's geometry, a key parameter is the aspect ratio B/D, defined as the ratio of the along-wind (B) to the cross-wind dimension (D). In smooth flow, depending on elongation, the shear layers separated from the leading edges may remain detached ($B/D < 2$), reattach on the side faces before merging with downstream vortices ($3.5 < B/D < 10$), or shed directly from the trailing edge in very elongated sections ($B/D > 10$) (Naudascher and Wang, 1993). These regimes correspond respectively to leading-edge vortex shedding (LEVS), impinging leading-edge vortex (ILEV), and trailing-edge vortex shedding (TEVS). LEVS and TEVS share similarities as both are governed by wake instabilities, where the shedding frequency relative to the flow velocity is nearly constant and primarily related to wake width (Griffin, 1978; Nakamura, 1996). In

* Corresponding author.
E-mail addresses: marcello.catania@polimi.it (M. Catania), giulia.pomaranzi@polimi.it (G. Pomaranzi), alberto.zasso@polimi.it (A. Zasso).
[1] Principal corresponding author.

https://doi.org/10.1016/j.jfluidstructs.2026.104538
Received 10 October 2025; Received in revised form 1 December 2025; Accepted 13 February 2026
Available online 25 February 2026

contrast, ILEV dynamics involve the interaction of vortices shed from both edges, with the Strouhal number strongly dependent on B/D (Païdoussis et al., 2010).

When the shedding frequency approaches one of the structural natural frequencies, synchronization (lock-in) occurs. Vortices couple with the motion, creating an effective forcing that amplifies oscillations until limited by damping. Structural damping, often expressed through the Scruton number $Sc = 4\pi m\xi/(\rho BD)$, thus governs the steady-state response (Williamson and Govardhan, 2004).

Several passive strategies have been proposed to mitigate VIV, mainly involving modifications to the structure's geometry or surface to disrupt the regular vortex shedding process without external energy input. They include tapering, to undermine the coherence of vortices along the height, cross-sectional modifications, often on edges, that can effectively reduce cross-wind oscillations by changing the separated shear layer characteristics (Kawai, 1998). Another possibility to affect the shear layer separation is to apply porous coverings to the structure (Teimourian and Teimourian, 2021): such elements can play a dominant role in altering the aerodynamic behavior of structures, either streamlined as bridge decks or bluff as towers or chimneys, being able to interfere with the generation of coherent vortices. Recent studies on porous-coated cylinders have shown that flow penetration through the coating weakens or delays shear-layer roll-up, broadens or destabilizes the wake, and can lead to substantial VIV reductions, especially when permeability is appropriately selected (Yuan et al., 2021).

In the construction industry, porous façades are gaining popularity primarily for architectural reasons or as thermal shading elements. When the porous screen is applied over a glazed façade, a so-called porous double-skin façade (PDSF) is created. Such cladding systems are increasingly employed in either low- and high-rise buildings to to enhance energy performance (Chan et al., 2009; Barbosa and Ip, 2014; Wang et al., 2020; Alqaed, 2022), yet they also alter wind-structure interaction (Pelletier et al., 2023; Eissa et al., 2025). Experiments have shown reductions in façade pressure and cross-wind loads due to porous coverings (Hu et al., 2017, 2019; Pomaranzi et al., 2020), and a decrease of spectral energy at the shedding frequency (Pomaranzi et al., 2022; Giachetti et al., 2025). These findings suggest that porosity can influence both VS and VIV, but its effectiveness in affecting the fluid-structure interaction and the underlying mechanism are still open points.

Evidence indicates that porous façades can reduce VIV above a Scruton threshold (Catania et al., 2024). However, their effectiveness is strongly dependent on the initial conditions: while oscillations may be suppressed when starting from rest, they can fully develop if the system is perturbed. This state-dependent behavior highlights a major knowledge gap: how porosity modifies wake development, vortex shedding, and the force dynamics that govern VIV onset and growth.

From a numerical perspective, explicit modeling of porous shrouds is computationally prohibitive, and past attempts have been limited to two-dimensional configurations with simplified turbulence treatment (Jafari and Alipour, 2021a,b). Homogenized approaches such as pressure-jump models (Xu et al., 2022a,b), Darcy-Forchheimer relations (Pomaranzi et al., 2020; Ansari and Naeeni, 2024), or custom implementations (Zhao, 2023) are widely adopted. While these methods reproduce global loads in static conditions, their validity in unsteady regimes has not been systematically assessed.

This study addresses these gaps by investigating how a porous envelope affects both the rigid-body aerodynamics and the aeroelastic response of a rectangular prism with aspect ratio $B/D = 3.33$, representative of a high-rise building. The work focuses on three main aspects. First, it examines how porosity modifies vortex shedding and the pressure distribution around the prism, clarifying the physical mechanisms introduced by the porous layer. Second, it evaluates whether homogenized CFD models, particularly the Darcy-Forchheimer formulation, can reliably reproduce these effects and thus serve as predictive tools for unsteady aerodynamics. Finally, it examines the aeroelastic response of the porous-covered prism, with a particular focus on the onset of VIV and the conditions under which oscillations are suppressed or maintained.

To assess these points, the paper is organized as follows. Section 2 introduces the methodology, including experimental and numerical approaches. Section 3 and 4 present the experimental setup and numerical implementation. Section 5 reports results on the rigid model and its numerical interpretation. Section 6 discusses the aeroelastic response under different initial conditions. Section 7 concludes the work and outlines further developments.

2. Methodology

The reference geometry is a rectangular cylinder with aspect ratio $B/D = 3.33$ and height ratio $H/B = 2$, representative of a high-rise building. This aspect ratio comes from a broader research using the same model geometry Pomaranzi et al. (2022), Catania et al. (2024), ensuring consistency across campaigns. Moreover, $B/D = 3.33$ contributes to expand the knowledge of less studied aspect ratios, greater than 1.5 but smaller than 4.5, suitable for civil applications.

Two configurations are examined: the naked prism and the same prism covered by a perforated metal shroud, adopted as a model for a porous façade. The study combines experimental and numerical approaches with the dual objective of clarifying the flow mechanisms induced by porosity and validating a numerical methodology for unsteady aeroelastic applications.

The first stage investigates how the porous envelope modifies vortex shedding (VS). A rigid three-dimensional model is tested in the wind tunnel, and results are compared with literature data to contextualize the observed wake dynamics. In parallel, a CFD model of a sectional prism is developed and validated for both naked and porous configurations. The computational domain is limited to a representative slice, located far from free-end effects, so that the focus remains on local shedding mechanisms governed by cross-sectional dynamics rather than spanwise boundary conditions. This approach also ensures computational efficiency, making Large-Eddy Simulations (LES) feasible while still resolving the unsteady features of the wake. Once validated against experimental measurements, the numerical model is used to interpret the physical mechanisms, providing insight into the pressure field on the inner façades and into the modifications introduced by porosity. This stage also establishes the reliability of the Darcy-Forchheimer homogenized model adopted for the porous treatment.

Table 1
Geometric and mechanical properties of the model in the two configurations. From left: along-wind (B) and cross-wind (D) dimensions, height (H), natural frequency in still air (f_1), equivalent modal mass per unit length (m_1), structural damping ratio (ξ) of the cross-wind vibration mode, and Scruton number (Sc).

Configuration	B [m]	D [m]	H [m]	f_1 [Hz]	m_1 [kg/m]	ξ [%]	Sc [-]
Naked	1.00	0.30	2.00	1.95	45.2	1.3	10.0
Porous	1.04*	0.34*	2.00	1.88	48.6	1.0	8.3

* Including the shroud dimensions. All non-dimensional quantities are calculated using the naked geometry as a reference.

The second stage focuses on aeroelastic response and the onset of vortex-induced vibrations (VIV). A scaled model with the same geometry and fixed mechanical properties is mounted on an elastic base, enabling direct comparison between naked and porous configurations. Building on previous evidence of Scruton number dependence and sensitivity to initial conditions (Catania et al., 2024), the tests explore the role of porosity in modifying VIV initiation. Since the phenomenon is inherently state-dependent, three types of initial conditions are examined: build-up (BU) tests starting from rest to capture the natural transition to lock-in; progressive-regime (PR) tests obtained by gradually increasing the wind velocity from a previous steady-state condition; and external-input (EI) tests starting in a stable condition and introducing a displacement perturbation. The objective is to assess how the porous shroud influences the initiation of VIV and to identify the force dynamics that govern the observed response.

The sectional CFD approach is tailored to capture vortex shedding and its modification by porosity, but it does not reproduce three-dimensional aerodynamic effects such as tip vortices or the aeroelastic VIV phenomenology. These aspects are instead addressed through complementary aeroelastic experiments on the finite-height model. Together, the two methodologies provide a consistent framework for linking rigid-body aerodynamics, flow physics, and VIV onset in porous-covered structures.

The following chapters describe in detail the experimental and numerical setups, before presenting the main results and discussing their implications for both aerodynamic characterization and aeroelastic response.

3. Experimental setup

The model is a rigid rectangular cylinder that can also be installed on an elastic base, allowing low-frequency mono-harmonic oscillations in the cross-wind direction. Two façade configurations are tested: a “naked” single-glazed cladding and a “porous” double-skin façade (Fig. 1). In the porous case, a perforated mesh with 55% porosity, defined as the ratio of empty to total area, is placed 20 mm from the solid façade. The mesh is characterized by round holes, 6 mm in diameter, organized in triangles with a center-to-center distance of 8 mm. The measured pressure loss coefficient of the mesh is $k = 1.8$, defined as

$$k = \frac{\Delta p}{0.5\rho U^2}, \tag{1}$$

where Δp is the total pressure difference across the porous medium. In the aeroelastic configuration, the model is characterized by a linear mode shape with respect to the equivalent bottom hinge, $\phi(z) = z/H$. Four accelerometers and 208 pressure taps, distributed across eight levels, are used to measure displacement and pressure variations (see the scheme in Fig. 2). The total cross-wind force acting on the structure is reconstructed as the sum of the local contributions at each level:

$$F_{\text{tot}}(t) = \sum_{i=1}^{8} F_i(t) = \sum_{i=1}^{8}\sum_{j=1}^{10} p_{i,j}(t)A_{i,j}, \quad [N] \tag{2}$$

where each floor force is obtained from the pressure integral on the lateral faces, with $A_{i,j}$ the reference area associated with tap j on floor i.

In the aeroelastic configuration, the effective forcing is computed by weighting each local force by the mode shape contribution at its height:

$$Q_{\text{tot}}(t) = \sum_{i=1}^{8} Q_i(t) = \sum_{i=1}^{8} F_i(t)\phi(z_i), \quad [N] \tag{3}$$

and thus the equation of motion for the top displacement becomes

$$M_1\ddot{x} + r_1\dot{x} + k_1 x = Q_{\text{tot}}(t), \quad [N] \tag{4}$$

with modal properties defined as $M_1 = \frac{m_1 H}{3}$, $r_1 = 4\pi M_1 f_1 \xi$, and $k_1 = M_1(2\pi f_1)^2$. The geometric and mechanical properties of both configurations are summarized in Table 3.

All tests are performed with the wind perpendicular to the short edge (D). The reference velocity is measured at 1 m height and 7 m upstream of the model. Experiments are conducted in the atmospheric boundary layer section of the Politecnico di Milano wind tunnel (GVPM), under smooth flow with turbulence intensity $I_u \approx 2\%$ (see flow characterization in Fig. 3). Further details on the model and facility are reported in previous studies (Pomaranzi et al., 2022; Catania et al., 2024).

Fig. 1. Model in the wind tunnel test section. Left: naked configuration and reference system. Right: porous configuration, zoom on the porous envelope.

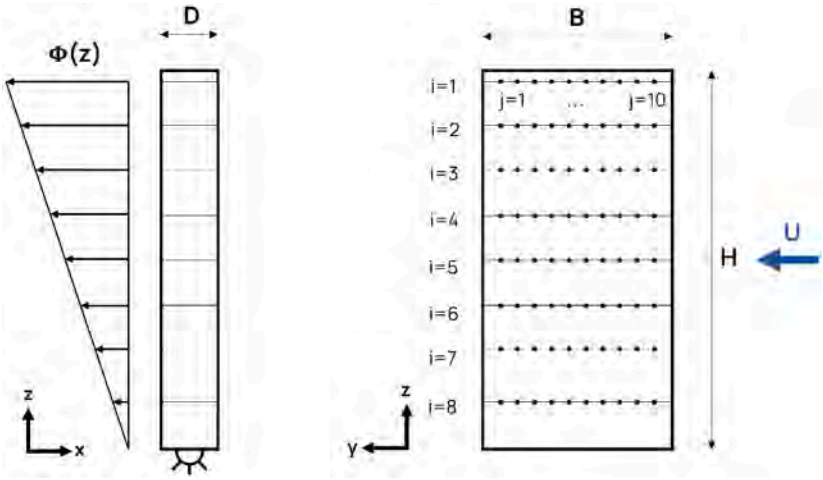

Fig. 2. Scheme of the tested model. Highlight of the building floors (numbered with letter i) and pressure taps distribution on the cross-wind faces (numbered with letter j).

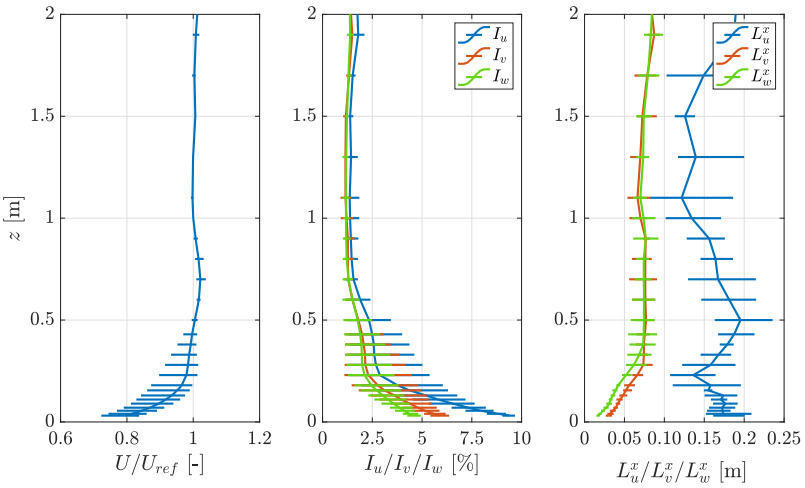

Fig. 3. Flow characteristics of GVPM BL test section in smooth flow condition. From left to right: model height against non-dimensional wind speed (U/U_{ref}), turbulence intensities (I_u, I_v, I_w), and integral length scales (L_u^x, L_v^x, L_w^x) in the three spatial directions.

4. CFD Setup

A set of Wall-Modeled Large Eddy Simulations (WMLES) is employed to investigate the effect of the porous façade on vortex shedding and to provide flow-field insight complementary to the experimental observations. This turbulence modeling has been chosen because it has been proven accurate in reproducing bluff body aerodynamics, allowing for capturing fine flow dynamics with less demanding mesh requirements compared to a standard LES, thus a lighter computational cost Franco et al. (2023). For a complete review of WMLES approaches, the authors indicate Piomelli (2008), Larsson et al. (2016).

In this study, the simulations focus on the rigid configuration, where the vortex-shedding dynamics are governed primarily by the cross-sectional geometry of the prism (Grozescu et al., 2011a; Alvarez et al., 2019). For this reason, only a sectional model of the building is reproduced numerically on 3D simulations, neglecting the finite-height effects. As commented in the next sections, floor 5 of the experimental model is selected as the reference for validation, being sufficiently far from end conditions to represent two-dimensional flow behavior.

Numerical methods

All simulations are carried out with the `pimpleFoam` solver of OpenFOAM-v2112, which combines the PISO and SIMPLE algorithms and is suited for unsteady, incompressible turbulent flows. The PIMPLE algorithm is configured with two outer correctors and three inner correctors, ensuring stability and convergence of the pressure-velocity coupling. Pressure is solved with a GAMG algorithm using Gauss-Seidel smoothing, while velocity is solved with a PBiCG method preconditioned with DILU.

A variable time step is used with a maximum Courant number of 0.8, corresponding to $\Delta t f_{VS} \approx 3 \times 10^{-5}$, i.e., more than thirty thousand time steps per vortex-shedding cycle. The adaptive time stepping automatically adjusts to the smallest cell sizes in the mesh, ensuring that the local Courant number remains below the prescribed limit and that temporal resolution is sufficient to capture the relevant unsteady flow features. In this way, the time-step control links the temporal resolution to the local flow convergence, simplifying the setup while maintaining numerical stability and accuracy.

Second-order accuracy is maintained in both space and time. The temporal discretization is based on a Crank-Nicolson scheme with an implicit weighting factor of 0.8. Spatial discretization employs linear interpolation schemes with flux limiting. Gradients are computed with a cell-limited Gauss linear scheme, while divergence terms are treated with a Gauss LUST (Linear Upwind Stabilized Transport) scheme, which provides stability while retaining low numerical dissipation in the shear layers (Cao and Tamura, 2016). Diffusion terms are discretized with a corrected Gauss linear scheme, and surface-normal gradients are corrected to account for mesh non-orthogonality.

The WALE subgrid-scale (SGS) model is adopted, with the eddy viscosity equation discretized using a linear scheme. This SGS model is widely used for bluff-body simulations and has been shown to reproduce unsteady pressure and force statistics with good accuracy (Grozescu et al., 2011b; Bruno et al., 2014; Franco et al., 2023).

Each simulation is advanced until statistical convergence is reached. The initial transient is discarded, and statistics are collected over at least 30 shedding cycles to ensure reliability of the mean and fluctuating quantities. Convergence of the time-averaged aerodynamic coefficients and shedding frequency is verified by monitoring their running averages.

Computational domain and boundary conditions

The computational domain is a rectangular box aligned with the incoming flow; the prism is modelled as a smooth surface with sharp edges. A sketch of the domain with a zoom on the model edges is reported in Fig. 4. The upstream, downstream, and lateral extents follow standard guidelines for bluff-body LES to avoid blockage and outlet interference (Bruno et al., 2014). In particular, the spanwise length has been selected to ensure the requirement of capturing three-dimensional shedding structures while minimizing computational costs (Grozescu et al., 2011a; Georgiadis and Mankbadi, 2015). The domain characteristics are summarized in Table 4.

Inflow conditions reproduce an ideal smooth flow with a uniform velocity profile, corresponding to the reference velocity in the wind-tunnel experiments. A no-slip condition is applied at the prism walls, while symmetry boundaries are used for the lateral faces of the domain to minimize spurious confinement effects. Periodicity is imposed in the spanwise direction.

For velocity, a fixed-value condition is applied at the inlet, and a zero gradient condition is imposed at the outlet. Slip boundaries are adopted at the top and bottom, while the front and back boundaries are defined as symmetry planes. At the prism surface, a no-slip condition is imposed.

For pressure, a zero-gradient condition is applied at the inlet and prism surface, while a fixed-value condition is prescribed at the outlet. Slip conditions are again used at the top and bottom, with symmetry at the front and back.

The subgrid viscosity field employs a `nutUSpaldingWallFunction` at the prism wall, consistent with the wall-modeled LES approach. At the other boundaries, calculated or zero-gradient conditions are used to ensure consistency with the velocity field.

This set of boundary conditions provides stable and physically consistent simulations, closely replicating the wind tunnel environment and enabling direct comparison with experimental measurements (Bruno et al., 2010, 2012). A sketch of the domain is reported in Fig. 4.

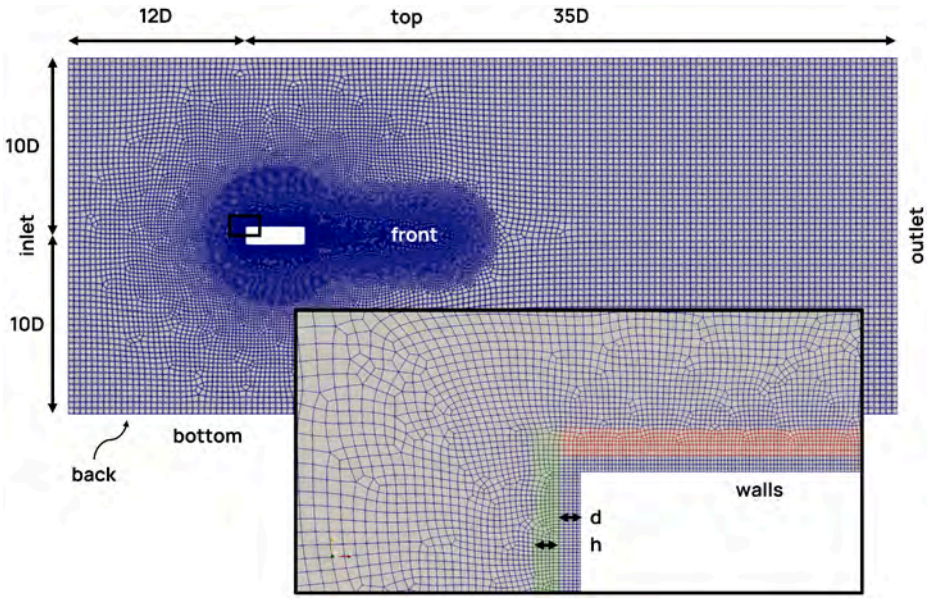

Fig. 4. Sketch of the meshed CFD with the main dimensions reported. Zoom of the prism's edge with the porous zones.

Table 2
Domain and mesh parameters adopted for the WMLES simulations. Values are expressed in terms of the cross-wind dimension D.

Parameter	Value	Comments / source
Upstream length	$12D$	avoids inflow blockage effects (Bruno et al., 2014)
Downstream length	$32D$	ensures wake development without outlet influence (Bruno et al., 2014)
Lateral clearance (side/top)	$9.5D$	prevents lateral confinement (Bruno et al., 2014)
Spanwise extent	$1D$	compromise between 3D resolution and cost (Georgiadis and Mankbadi, 2015)
Mesh type	Mostly unstructured	recommended for complex bluff-body wakes (Cao and Tamura, 2016)
Total cells	~ 4 million	satisfies resolution criteria for WMLES (Pope, 2000)
Near-wall resolution	$y^+ \approx$ 30-50	consistent with WMLES practice (Larsson et al., 2016)
Streamwise spacing	$\Delta x/D = 0.01$	ensures vortex shedding resolution (Kawai and Larsson, 2012)
Cross-wind spacing	$\Delta y/D = 0.01$	ensures shear layer resolution (Kawai and Larsson, 2012)
Spanwise spacing	$\Delta z/D = 0.01$	resolves 3D vortex structures (Kawai and Larsson, 2012)
Time step	$\Delta t f_{VS} \approx 3 \times 10^{-5}$	~33.333 steps per shedding cycle (Grozescu et al., 2011a)
Simulation length	$>$ 30 shedding cycles	sufficient for statistical convergence
Subgrid model	WALE	effective for bluff-body LES (Franco et al., 2023)

Mesh generation

A body-fitted hybrid mesh is adopted, with refinement in the near-wake and along the prism edges, where accurate resolution of the shear layers is crucial (Rocchio et al., 2020; Yang et al., 2025). The grid is structured along the spanwise direction z and mostly unstructured in the x-y plane; around the cylinder walls, a structured grid layer of 6 cells with an expansion ratio of 1.05 is generated. The discretization step perpendicular to the walls is $\Delta y/D = 0.01$, while a constant grid spacing of $\Delta x/D = 0.01$ is adopted in the along-wind direction. Near the walls, the mesh size is chosen according to the guidelines of (Piomelli, 2008) to ensure results convergence in a statistical sense. Grid stretching is employed in the far field to reduce computational cost. A refinement zone in the wake 9D immediately downwind of the model has been imposed to capture near wake vortices correctly. The 3D grid is obtained by projecting the 2D hybrid grid along the spanwise direction z. A constant spacing has been imposed at $\Delta z/D = 0.01$, smaller than the minimum requirement prescription for LES ($\Delta z/D \simeq 0.2$ by (Tamura et al., 1998; Yu and Kareem, 1998)).

The mesh density in the streamwise, crosswise, and spanwise directions is selected to guarantee the resolution of at least 80% of the turbulent kinetic energy in the domain, as prescribed by Pope (2000).

The effect of grid resolution has been investigated by comparing three meshes of increasing density, with refinement concentrated near the prism and in the near-wake region. All the tested meshes are characterized by $y^+ \simeq 30 - 50$ at the walls, compatible with wall-modeled LES best practices (Larsson et al., 2016), and respect the Pope criterion in the wake.

Key aerodynamic quantities, namely the mean drag coefficient $C_{D,m}$, the fluctuating lift coefficient $std(C_L)$, and the Strouhal number St were monitored (Table 4). Variations between the intermediate and finest meshes remained below 1% for $C_{D,m}$ while the shedding frequency was unaffected. The observed 13% variation in $std(C_L)$ is consistent with the natural sensitivity of fluctuating

Table 3
Grid independence and convergence study for naked model. Characteristics of the tested meshes and results comparison at $U = 4\,m/s$.

Mesh name	Mesh size	$C_{D,m}$	$std(C_L)$	St
M1 – coarse	~ 3 million	1.12	0.33	0.151
M2 – medium	~ 4 million	1.12	0.36	0.151
M3 – fine	~ 6 million	1.13	0.41	0.151

lift to spanwise resolution in WMLES. Similar levels of variation are reported for rectangular cylinders in Grozescu et al. (2011a), Alvarez et al. (2019). The mean values and shedding frequency, which are more robust indicators of mesh adequacy, confirm that the adopted mesh is sufficiently resolved for the purposes of the study.

Statistical convergence was verified by monitoring running averages of global force coefficients and shedding frequency, which reached stable values within the chosen sampling window (more than 30 shedding cycles). The final grid design (mesh M2) balances accuracy and computational feasibility. The adopted mesh parameters are summarized in Table 4.

The numerical model is validated against the experimental results through comparison of both local and global quantities. Local validation relies on the pressure coefficient defined as:

$$C_p(t) = \frac{p(t) - p_{ref}}{0.5\rho U^2}, \tag{5}$$

where $p(t)$ is the instantaneous surface pressure and p_{ref} is the static reference pressure.

Global aerodynamic forces are expressed through the non-dimensional force coefficient:

$$C_F(t) = \frac{F(t)}{0.5\rho U^2 Bh}, \tag{6}$$

where $F(t)$ is the aerodynamic force in either drag or lift direction, B is the along-wind dimension of the prism, and h its spanwise extent (equal to the thickness t for a sectional model).

The vortex shedding frequency f_{vs} is identified as the dominant peak in the power spectral density of the cross-wind force. The corresponding Strouhal number is then calculated as:

$$St = \frac{f_{vs} D}{U}, \tag{7}$$

where D is the cross-wind dimension and U the inflow velocity.

Validation is carried out by comparing the temporal mean and standard deviation of these quantities between CFD and wind tunnel results across the tested wind speed range. Agreement in pressure distributions, global force coefficients, and shedding frequency provides confidence in the numerical model and its ability to reproduce the key flow and force features of both the naked and porous configurations.

Porosity treatment

The effect of the porous envelope is modeled using the Darcy–Forchheimer approach, implemented in four mesh regions where an additional momentum sink is applied (see detail in Fig. 4). A thickness of more than 5 cells is ensured to guarantee that imposed momentum loss (Pomaranzi et al., 2021). This homogenized representation is appropriate since the characteristic pore size of the perforated sheet is much smaller than the global body dimensions (Xu et al., 2022a).

In these porous regions, a sink term $\mathbf{s} = [s_x, s_y, s_z]'$ is added to the momentum equation and defined according to the Darcy–Forchheimer law as

$$\mathbf{s} = -\mu \mathbf{D}\mathbf{u} - \tfrac{1}{2}\rho U \mathbf{F}\mathbf{u}, \tag{8}$$

where $\mathbf{u} = [u_x, u_y, u_z]'$ is the local velocity vector, $U = \|\mathbf{u}\|$ its magnitude, μ and ρ are the fluid viscosity and density, and $\mathbf{D}$ and $\mathbf{F}$ are diagonal matrices representing the Darcy and Forchheimer tensors.

Since the envelope consists of a perforated metal sheet, viscous stresses (the Darcy term) are negligible and the dominant interaction is due to pressure drag (Pomaranzi et al., 2021). For incompressible flow, the momentum equation therefore reduces to

$$\frac{\partial u_i}{\partial t} + \frac{\partial (u_j u_i)}{\partial x_j} = \frac{\partial}{\partial x_j}\left(\mu \frac{\partial u_i}{\partial x_i}\right) + \frac{1}{\rho}\frac{\partial p}{\partial x_i} - \tfrac{1}{2} U f_i u_i, \qquad i, j = x, y, z, \tag{9}$$

where p is the pressure and f_i are the diagonal terms of the Forchheimer tensor

$$\mathbf{F} = \begin{bmatrix} f_x & 0 & 0 \\ 0 & f_y & 0 \\ 0 & 0 & f_z \end{bmatrix}.$$

Because of the geometric symmetry of the perforated mesh, $f_y = f_z$. The normal resistance f_x is obtained by dividing the experimentally measured pressure-loss coefficient k by the porous domain thickness h. The tangential resistance coefficients f_y and f_z, not

directly measurable, are estimated following the methodology of Marykovskiy et al. (2024) and Pomaranzi et al. (2021), which compares forces from explicit and homogenized porous-medium models. The resulting ratio $f_y = f_z \simeq f_x/13$ is consistent with previous high-fidelity CFD studies on similar perforated materials (Marykovskiy et al., 2024; Chen and Christensen, 2016).

5. Rigid model results

The analysis begins with the rigid configuration. Wind-tunnel tests were carried out to characterize the pressure distribution on the prism's inner façade in both the naked and porous configurations, to highlight the aerodynamic differences between the two. Measurements were repeated at five wind velocities ($U = [3, 4, 5, 6, 8]\, m/s$) to verify the consistency of the results across different Reynolds numbers. Experimental data were first used to validate the CFD model, which was subsequently employed to gain further insight into the vortex-shedding (VS) mechanism and the flow modifications induced by the porous envelope.

Aerodynamic characterization

Figs. 5 report the mean pressure coefficient $C_{p,m}$ (subfigures a,c) and its standard deviation $std(C_p)$ (subfigures b,d) for the naked and porous configurations. Since the results are independent of wind speed, only the case at $U = 4\, m/s$ is shown. In the plots, façade A denotes the windward surface perpendicular to the incoming flow, B and D represent the lateral faces, and C corresponds to the leeward face.

In both configurations, the windward surface exhibits a mean pressure coefficient close to unity with negligible fluctuations, as expected for a stagnation region.

For the naked configuration (Figs. 5a,b), the leeward face C is characterized by a coherent negative pressure region associated with the formation of a recirculation bubble. On the central floors (3-4-5-6), $std(C_p)$ reaches a minimum near the mid-width tap and peaks at the outer taps, a signature of the alternating von Kármán vortex pair. Along the lateral façades, a nearly constant negative pressure region develops near the leading edge ($C_{p,m} \simeq 0.8$, $std(C_p) \simeq 0.04$). Moving downstream, the mean pressure partially recovers ($C_{p,m} \simeq 0.3$) and pressure fluctuations increase ($std(C_p) \simeq 0.14$). This behavior reflects the dynamics of the separated shear layer, which reattaches downstream, causing a partial pressure recovery and stronger unsteady loading. Minor asymmetries are visible between faces B and D, likely due to a slight model misalignment with respect to the incoming flow, though they do not significantly affect the overall phenomenology.

A clear variation of pressure distribution along the height is observed. Three-dimensional effects at the clamped and free ends cause an earlier reattachment of the shear layer and a smaller negative pressure bubble at the extremities. These end effects, typically associated with the formation of horseshoe and tip vortices, are well documented in literature (Rastan et al., 2021; Sumner et al., 2017). Consequently, floors 4-5-6 show the most uniform pressure distribution, being less influenced by boundary conditions, and are therefore selected as reference sections for the validation of the sectional CFD model.

In the porous configuration (Figs. 5c,d), a similar global pattern is observed, but the magnitude of both mean and fluctuating pressures is considerably reduced. The lateral façades display an almost constant $C_{p,m}$, with an average decrease of about 40% compared to the naked case. The amplitude of $std(C_p)$ near the leeward edge is also reduced by roughly 35%, indicating a weaker wind-structure interaction. Moreover, the pressure field is more uniform along the height, with less pronounced three-dimensional effects. This homogenization of pressure and reduction in fluctuation intensity confirm the filtering effect of the porous medium on the aerodynamic loads.

Being the VS mainly affected by the cross-sectional geometry, and to isolate the role of the porous covering on VS from edge effects, the analysis is restricted to the central floors (4-5-6). Since they exhibit a similar behavior in the experiments, floor 5 is chosen as a reference for the comparison with CFD results.

For the naked configuration, numerical and experimental results show good overall agreement in both mean and fluctuating pressure distributions (Figs. 6a–b). The most noticeable discrepancies occur around $y \approx 0.8D$ on the cross-wind faces and at the leeward edge, where the CFD slightly overestimates suction. These deviations are consistent with known differences between sectional CFD models and finite-height experiments. In the wind-tunnel setup, end-induced structures such as tip downwash and horseshoe vortices reduce the extent of the recirculation bubble and weaken the leeward suction (Rastan et al., 2021; Sumner et al., 2017), leading to reduced mean pressure values compared to the sectional models. Likewise, the interaction between primary and secondary tip vortices disrupts the coherence of the shear-layer roll-up along the height, producing a smoother $std(C_p)$ distribution experimentally, while the sectional CFD preserves full spanwise coherence and thus predicts a more pronounced fluctuating peak (Bruno et al., 2014; Grozescu et al., 2011a).

Differences in inflow conditions further contribute to the mismatch: the CFD adopts a smooth inflow, whereas the wind-tunnel tests exhibit a turbulence intensity of about 2% with integral scales of 15–20 cm (Fig. 3). As shown in (Ricci et al., 2017; Alvarez et al., 2019), such turbulence accelerates wake recovery and reduces both leeward suction and fluctuating loads, consistent with the experimental trends.

Despite these localized discrepancies, global aerodynamic coefficients (drag, lift, Strouhal number) remain fully consistent with the measurements and with reference data for similar geometries (Sohankar, 2008; Wang et al., 2024), confirming that the sectional CFD model captures the dominant vortex-shedding behaviour.

For the porous configuration, the agreement between CFD and experiments is considerably stronger. Both the mean and fluctuating pressure distributions (Figs. 6c–d) follow the measured trends closely, with deviations markedly smaller than those observed in the naked case. The CFD reproduces the experimentally observed reduction in suction on the side and leeward façades and the

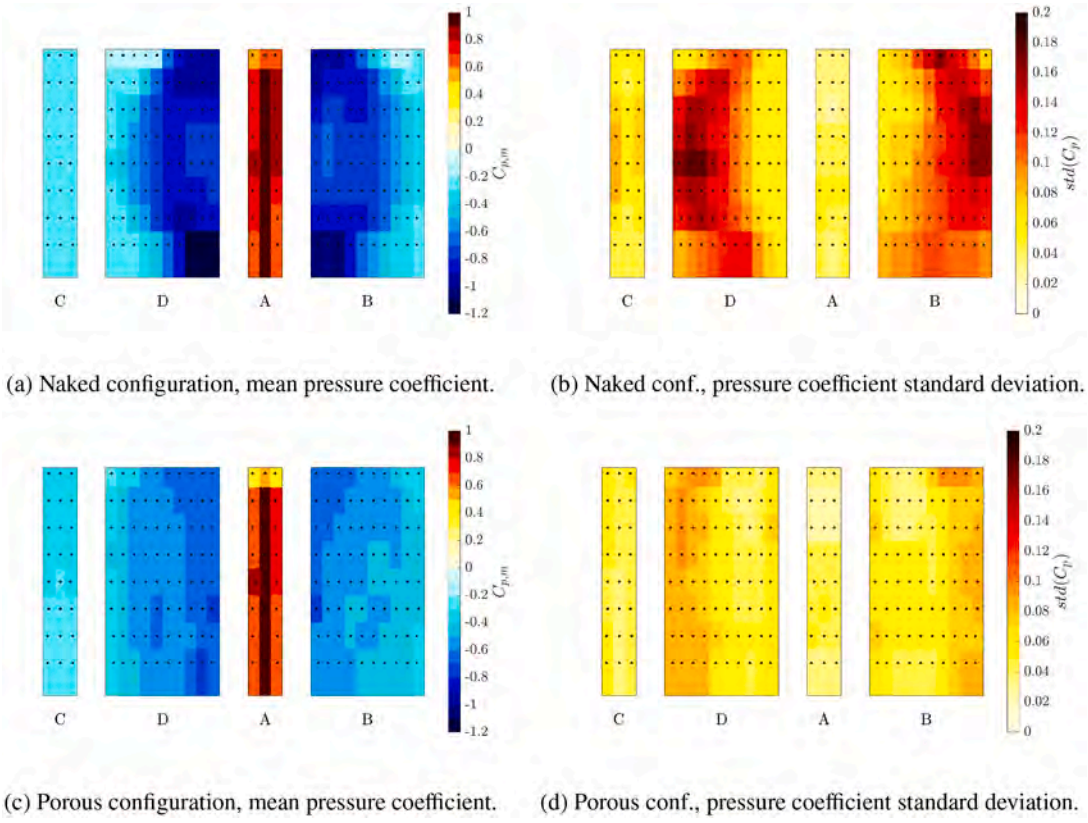

(a) Naked configuration, mean pressure coefficient.

(b) Naked conf., pressure coefficient standard deviation.

(c) Porous configuration, mean pressure coefficient.

(d) Porous conf., pressure coefficient standard deviation.

Fig. 5. 3D structure, $U = 4\,m/s$.

Table 4
Comparison between experimental and numerical aerodynamic quantities on a section of the rectangular cylinder. The statistics are obtained from tests on the rigid model at $U = [3, 4, 5, 6, 8]\,m/s$. In the experimental results, just floors 3,4,5 are considered.

Source	Configuration	B/D [−]	$C_{D,m}$ [−]	$std(C_D)$ [−]	$std(C_L)$ [−]	St [−]
Present study	Naked-Exp.	3.33	1.10±0.01	0.079±0.049	0.25±0.05	0.138±0.016
Present study	Naked-CFD	3.33	1.13±0.03	0.054±0.006	0.35±0.03	0.151±0.020
Present study	Porous-Exp.	3.33	1.12±0.01	0.058±0.036	0.17±0.04	0.038±0.020
Present study	Porous-CFD	3.33	1.40±0.17	0.040±0.023	0.22±0.12	0.055±0.007
Shimada and Ishihara (2002)	Naked-CFD (RANS)	3.5	1.23	–	≃ 0.4	0.140-0.155
Sohankar (2008)	Naked-CFD (LES)	3.5	1.2	0.02-0.1	≃ 0.5	0.150
Yu and Kareem (1998)	Naked-CFD (LES)	4	≃ 1.35	–	1	≃ 0.155
Alvarez et al. (2019)	Naked-CFD (LES)	4	1.03-1.14	0.04-0.10	0.31-0.90	0.131-0.142
Wang et al. (2024)	Naked-CFD (LES)	4	1.07	0.05	0.53	0.137
Yu and Kareem (1998)	Naked-CFD (LES)	3	1.30	–	1	≃ 0.185
Shimada and Ishihara (2002)	Naked-CFD (RANS)	3	1.15-1.20	–	0.1-0.4	0.165

attenuation of the pressure fluctuations associated with the filtered shear-layer dynamics. This improved match indicates that the Darcy–Forchheimer homogenized model accurately captures the aerodynamic influence of the porous envelope, including its capacity to redistribute pressure and weaken the unsteady loading on the inner façade. The consistency between numerical and experimental results provides confidence in the suitability of this modelling approach for interpreting the flow mechanisms induced by porous façades.

Comparison with literature

The aerodynamic properties of the $B/D = 3.33$ section fall between those of $B/D = 3$ and $B/D = 4$ prisms. Reported Strouhal numbers range from 0.185 (Yu and Kareem, 1998) to 0.165 (Shimada and Ishihara, 2002) for the aspect ratio 3 and from 0.131-0.142 (Alvarez et al., 2019) to 0.137 (Wang et al., 2024) for aspect ratio 4, with values around 0.150 for $B/D = 3.5$ (Sohankar, 2008). Mean drag coefficients vary between 1.23 (Shimada and Ishihara, 2002) and 1.03-1.14 (Alvarez et al., 2019), while the

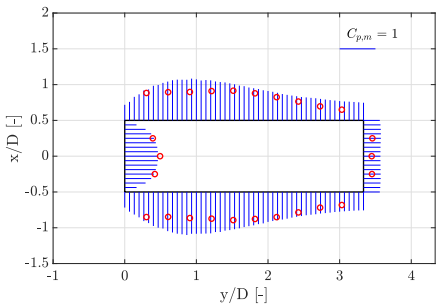

(a) Naked configuration, mean pressure coefficient.

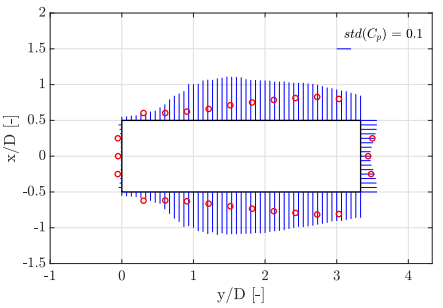

(b) Naked conf., pressure coefficient standard deviation.

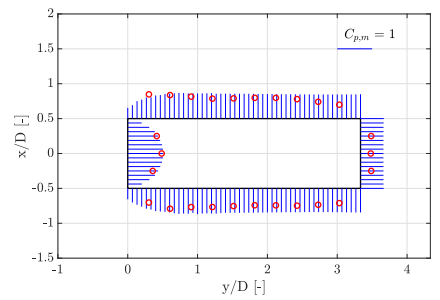

(c) Porous configuration, mean pressure coefficient.

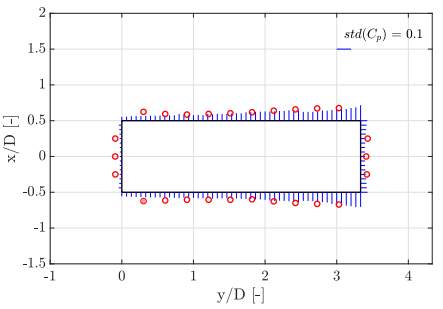

(d) Porous conf., pressure coefficient standard deviation.

Fig. 6. Floor 5, $U = 4\,m/s$. Red dots: experimental results, blue bars: CFD results. (For interpretation of the references to colour in this figure legend, the reader is referred to the web version of this article.)

standard deviation of drag lies between 0.02 and 0.1 (Sohankar, 2008), and the fluctuating lift ranges between the minimum of 0.1 (Shimada and Ishihara, 2002) to the maximum of 1.0 (Yu and Kareem, 1998). The present results (Table 5) fall within these ranges, confirming the accuracy of both experimental and numerical approaches.

Flow modifications induced by porosity

Streamline visualizations reveal an additional separation point at the porous layer edge, generating a broader low-pressure zone and a larger downstream recirculation region (see comparison between Fig. 7a–b and detail (c)). A secondary recirculation bubble forms through the porous shroud, producing confined-flow behavior on the structural façade (see Fig. 7d). In this region, nearly parallel streamlines lead to a uniform pressure distribution in the along-wind direction (Deville, 2022). This explains the homogenization effect observed in the cross-wind façades: both $C_{p,m}$ and $std(C_p)$ are flatter and more uniform than in the naked case. As a consequence, the porous façade reduces the mean and oscillating pressure on the inner surface by up to 40% (Fig. 6), consistent with previous findings on porous shielding devices (Pomaranzi et al., 2020).

Vortex shedding characterization

Vortex shedding dynamics are characterized by analyzing the frequency of the cross-wind force. Slight discrepancies among levels are observed, mainly at the floors 6-7-8, due to the boundary layer in the wind tunnel, which reduces local mean velocity (Fig. 3). The Strouhal number, however, remains nearly constant across levels. Two dominant frequencies are detected: a low-frequency branch at $St = 0.033 \pm 0.017$, associated with detached shear layers, and a high-frequency branch at $St = 0.138 \pm 0.016$, linked to reattached shear layers. Such dual behavior is typical of rectangular cylinders with $2.5 < B/D < 3.5$, which fall in a critical regime where both separated-flow and reattachment modes can coexist (Zdravkovich, 1997; Wang and Zhou, 2009; Rastan et al., 2017).

The CFD results capture both behaviors, showing peaks at $St = 0.014$ and $St = 0.127$–0.145, consistent with the mid-level experimental data (Fig. 8). The dominant VS mode relevant for VIV corresponds to the reattached-flow branch, as discussed in the following section.

In the porous configuration, two peaks are also identified: the main one at $St = 0.055 \pm 0.007$, originating from shear layer separation at the porous envelope edge, and a secondary one at $St = 0.124 \pm 0.011$, slightly lower than in the naked case.

To characterize wake dynamics in a non-dimensional and physically consistent manner, both the spanwise vorticity and the Q-criterion are reported in normalized form:

$$\omega_z^* = \frac{\omega_z D}{U}, \qquad Q^* = \frac{Q D^2}{U^2}.$$

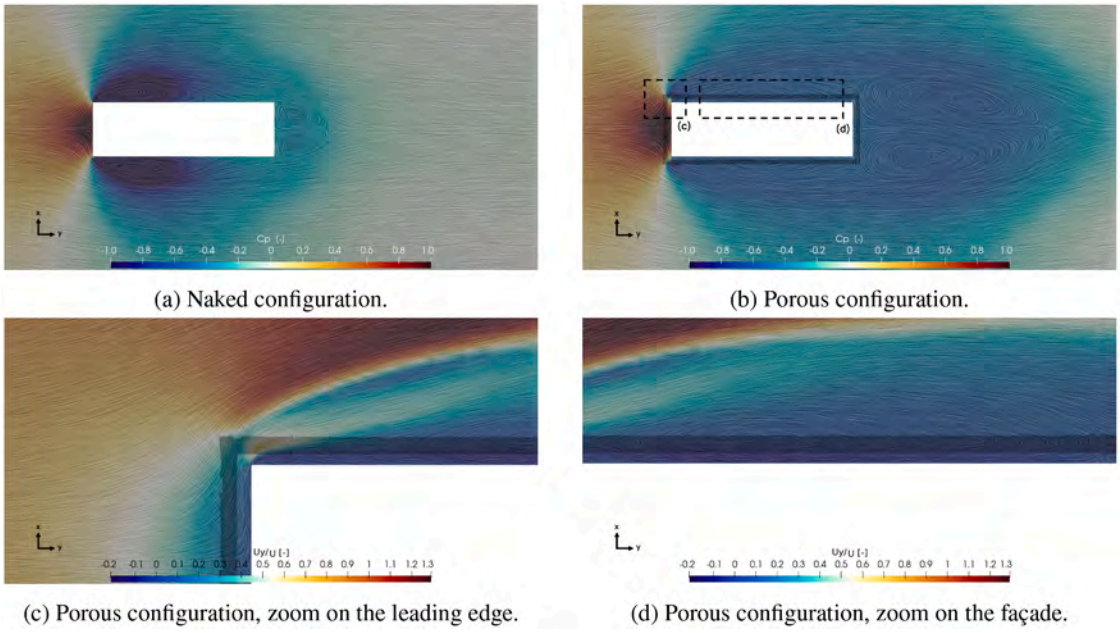

Fig. 7. Streamline representation of the mean velocity field $U = 4\,m/s$. On the background normalized pressure C_p in the top figures and normalized flow velocity in the along-wind direction U_y/U in the bottom figures.

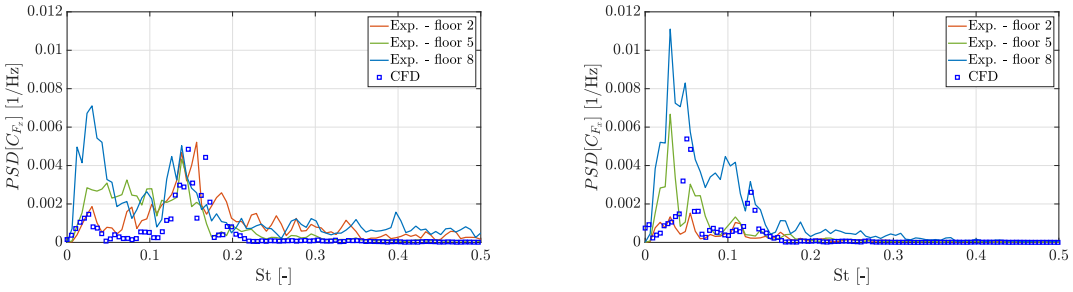

Fig. 8. Comparison between the power spectral density of the force coefficients measured at floors 2,5,8 (colored lines) and the one calculated from the CFD simulation (blue squares) at $U = 4\,m/s$. (For interpretation of the references to colour in this figure legend, the reader is referred to the web version of this article.)

The scaling removes the dependence on the absolute velocity magnitude U, enabling a consistent comparison between the naked and porous configurations and highlighting coherent structures across different flow regimes (Jeong and Hussain, 1995).

Using these normalized quantities, Fig. 9 shows that vortices shed from the porous-layer edges (Fig. 9b detail (1)) interact downstream with those generated at the structural façade (Fig. 9b detail (2)), producing a broader wake. Iso-surfaces of Q^* capture the interaction and merging of the two shedding systems, which leads to large-scale wake meandering. This modulation correlates strongly with the low-frequency force component at $St \approx 0.055$, indicating that the porous façade introduces a distinct low-frequency shedding mode that dominates the aerodynamics of the modified configuration.

6. Aeroelastic results

The rigid-model analysis established that the porous façade modifies vortex shedding by introducing an additional low-frequency mode and homogenizing the pressure distribution on the inner surfaces. The next step is to evaluate whether these aerodynamic changes affect the onset and development of aeroelastic instability. To this end, the structure is now allowed to oscillate freely under cross-wind excitation. Building on the previous experimental findings Catania et al. (2024), the Scruton number is selected within the range where porosity effectiveness has been shown to be strongly state-dependent. This results in $Sc = 10$ for the naked configuration and $Sc = 8.1$ for the porous configuration. The focus is therefore the investigation of different VIV onset mechanisms, depending on initial conditions, and the way they are affected by the presence of the porous covering.

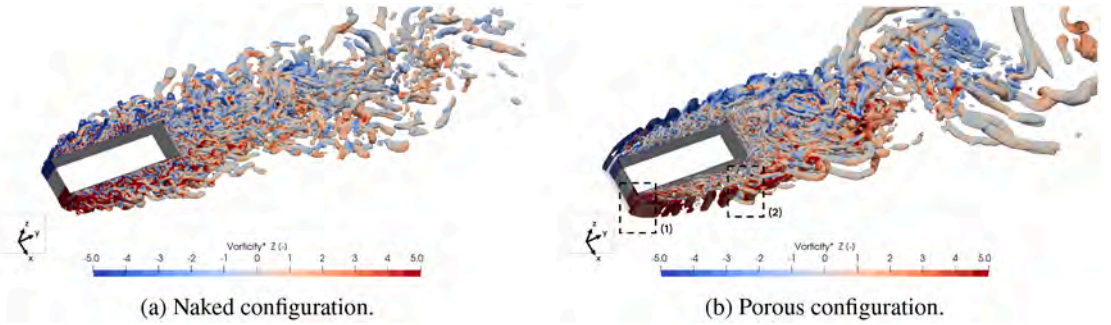

(a) Naked configuration. (b) Porous configuration.

Fig. 9. Instantaneous isosurface of $Q^* = 1$, color map by non-dimensional vorticity magnitude in the z-direction. $U = 4\,m/s$.

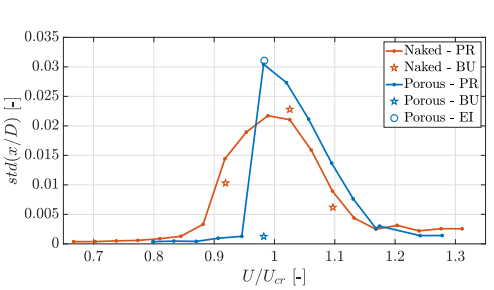

(a) Non-dimensional displacement standard deviation $std(x/D)$.

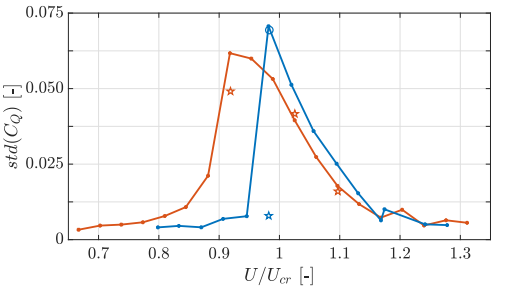

(b) Lagrangian force coefficient standard deviation $std(C_F)$.

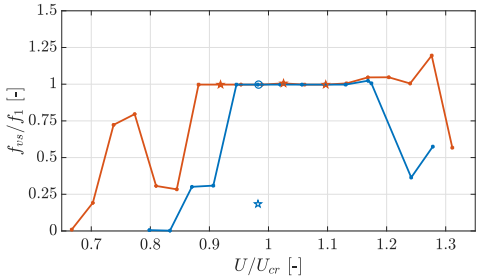

(c) Non-dimensional vortex shedding frequency f_{vs}/f_1.

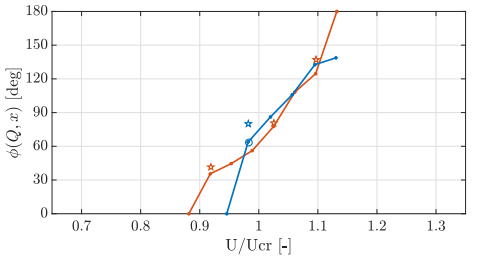

(d) Phase between total force and displacement $\phi(F, x)$.

Fig. 10. Bell-shaped plot of the characteristic VIV quantities against non-dimensional wind speed U/U_{cr}. Naked configuration (orange), porous configuration (blue). (For interpretation of the references to colour in this figure legend, the reader is referred to the web version of this article.)

To investigate the vortex-shedding, cross-wind displacement, and pressure distribution over the model external surface are monitored, increasing the wind speed from $0.65U_{cr}$ to $1.3U_{cr}$, where U_{cr} is the wind speed at which $f_{VS} = f_1$. Results are summarized in Fig. 10, where subplot (a) reports the standard deviation of the cross-wind displacement measured at the top of the building as a function of the wind speed, while subplot (b) shows the oscillations of the Lagrangian component of lift force, obtained from pressure integration over the lateral surfaces of the model multiplied by the mode shape evaluated at each section (as indicated in Eq. 3). To fully characterize the VIV phenomenon, the VS frequency is obtained from the lift force and monitored as a function of the wind speed, as shown in subplot (c). Finally, the phase shift between the total lateral force and the top displacement is reported in subplot (d). Fig. 10 collects the results obtained for the naked and PDSF configurations, both in progressive regime and build-up. All the quantities are evaluated in the steady-state conditions.

Naked configuration

Independent of the initial conditions, the naked configuration exhibits the canonical VIV behavior, with a well-defined lock-in region in the range $U = [0.9\text{-}1.2]\,U_{cr}$. In steady-state conditions, maximum oscillation amplitude occurs at $U = 0.98\,U_{cr}$, close to the critical velocity defined as $U_{cr} = f_1 D/St$. The aerodynamic force peaks slightly earlier, at $U = 0.95\,U_{cr}$, reproducing the characteristic bell-shaped response curve.

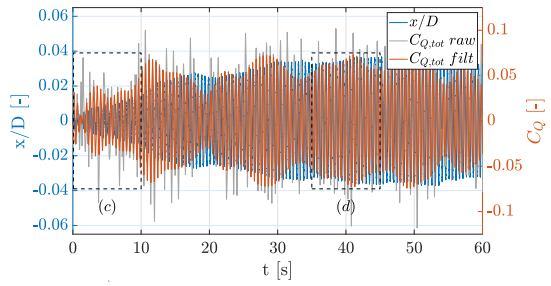

(a) Displacement and total force coefficient time history.

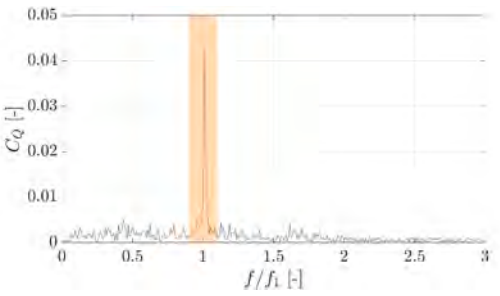

(b) Spectrum of the total force coefficient.

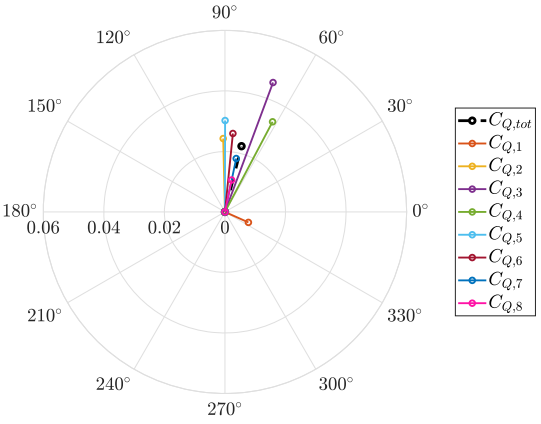

(c) Polar plot, zoom $t = [0, 10]$ s, rising VIV.

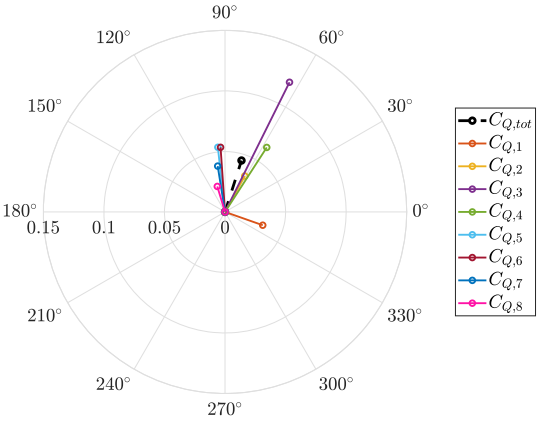

(d) Polar plot, zoom $t = [35, 45]$ s, fully developed VIV.

Fig. 11. Naked configuration, $U/U_{cr} = 1.02$, Build-up (BU).

Within the synchronization range, the aerodynamic force and structural displacement are nearly in phase, with a shift that grows with velocity. In this regime, the vortex-shedding frequency locks into the structural frequency, concentrating the energy of the aerodynamic forcing around f_1 (Fig. 10c). At $U \simeq U_{cr}$, the signals reach quadrature, a condition associated with maximum energy transfer and thus large-amplitude oscillations. Beyond this point, the phase shift increases toward 180°, marking the end of the lock-in region. This phenomenology is consistent with classical VIV theory (Williamson and Govardhan, 2004).

Since the focus is on the understanding of the VIV onset, it is of interest to analyze the transient to the steady-state conditions. To do so, build-up tests have been performed to understand the way steady-state conditions are reached from rest. Within the transient, it is interesting to monitor the evolution of aerodynamic force amplitude and phase with respect to the structural motion. Specifically, the pressure taps distributed along the model surface allow for the time-space reconstruction of the aerodynamic force, that, properly weighted by the modal shape $\phi(z)$, allows for the computation of the Lagrangian components of the external force and thus the identification of the levels that play a major role in the VIV phenomenon. The distinction between physical and modal forces is essential in this scenario, given the aero-elastic nature of VIV.

As an example, the tests at the most critical VIV condition, $U = 0.98\,U_{cr}$, are examined. For this case, Fig. 11a shows the time histories of the top displacement and of the total force coefficient in build-up conditions for the naked configuration. The force signal is represented both raw (grey line) and band-pass filtered between $0.9f_1$ and $1.1f_1$ (orange line). This comparison helps to highlight the state-dependent component and isolate it from the other spectral contributions. Fig. 11b displays the complete force spectrum instead, with a clearly visible peak at the resonance frequency.

During the transient, for the excitation to be effective, a Lagrangian component of the cross-wind force should be in quadrature with the structural displacement. This allows efficient energy transfer from the flow to the structure, promoting vortex-induced vibrations onset Ramesh et al. (2025).

The behavior of the Lagrangian components associated with different levels in the model can be conveniently visualized through polar plots: the vector length corresponds to the standard deviation of the Lagrangian component of the modal force at a given floor, while the angular position indicates its phase relative to the structural motion. In this representation, effective contributions appear as long vectors and in quadrature with respect to the displacement, whereas ineffective (out-of-phase or incoherent) components appear shorter or scattered. Referring to the time histories reported in Fig. 11a and considering the first oscillation cycles (0-10s), the polar plot of the Lagrangian components for each floor is presented in Fig. 11c, together with the total Lagrangian component. It results that the top floor ($C_{Q,1}$) is the only one characterized by a phase shift almost null, most likely due to the edge effects, while

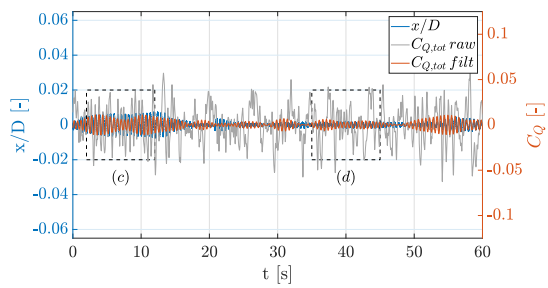

(a) Displacement and total force coefficient time history.

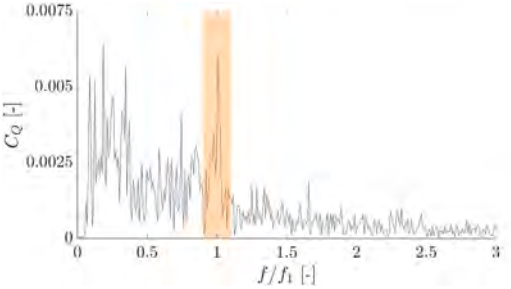

(b) Spectrum of the total force coefficient.

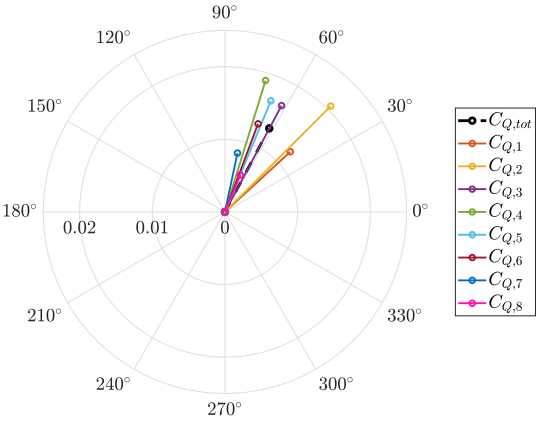

(c) Polar plot, zoom $t = [2, 12]$ s, rising VIV.

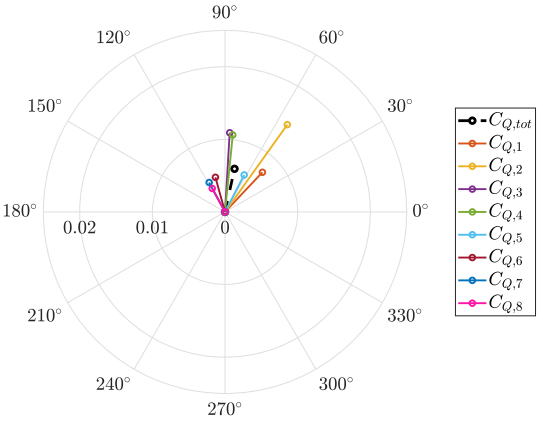

(d) Polar plot, zoom $t = [35, 45]$ s, no VIV.

Fig. 12. Porous configuration, $U/U_{cr} = 0.98$, build-up (BU).

all the other floors' contributions display coherent phases between 60° and 90°. This early-phase alignment efficiently injects energy into the system, and the resulting $C_{Q,tot}$ shares the same orientation as most of the floors.

Eventually, when the transient ends and VIV is fully developed, the force characteristics converge to steady-state. Fig. 11d shows the polar plot of the forces extracted in the time span 35-45s from Fig. 11a. The total forcing has the same phase observed in Fig. 10d: here level 3 provides the dominant contribution, followed by levels 2 and 4; higher floors show larger phase shifts, and the lowest floor is still strongly affected by end effects.

Porous configuration

Switching to the porous configuration, it is useful to go back to the steady-state plots reported in Fig. 10. The aeroelastic response changes markedly with respect to the naked configuration, showing a strong dependency on the imposed initial condition. In a progressive regime, VIV phenomenology is comparable to the naked case, with the characteristic 'bell-shaped plots' occurring at the $U/U_{cr} > 0.98$. Conversely, at the same critical wind speed $U/U_{cr} = 0.98$, no significant oscillations are recorded in the build-up case. To further understand this condition, Fig. 12a reports the time histories of the system response and the integral of the pressure field, expressed as modal force. The displacement is characterized by a pulsating behavior, with some cycles in which it seems to increase, followed by other periods with much smaller amplitudes. Given the aeroelastic nature of the force, the same behavior is manifested at the same time spans by the motion-induced component of the forcing. In fact, the force spectrum (Fig. 12b) reveals two main contributions: (i) a *motion-induced* component at the structural frequency $f = f_1$, corresponding to the natural oscillation mode; and (ii) a *porosity-induced* component at $f \simeq 0.3 f_1$ ($St \simeq 0.05$), consistent with the rigid-model results. In this case, the low-frequency forcing generated by the shroud edges cannot excite the natural frequency, and VIV does not develop.

Polar plots again provide insight into the spatial distribution of forces and their effectiveness on the VIV mechanism. Still referring to the most critical VIV condition, time ranges where the resulting Lagrangian components are characterized by the highest amplitudes are selected: Fig. 12c reports the polar plot from time range 2-12s. Different contributions are spread between 40° and 85°, with dominant contributions from top floors with opposing trend: levels 1 and 2 are contributing almost equally to levels 3-4-5 but they are consistent in phase behavior. This lack of coherence disrupts synchronization and prevents the establishment of lock-in. To further visualize this, the spectra of the Lagrangian components at such floors are shown in Fig. 14a: energy appears distributed over a broad range with main contributions at $St \simeq 0.05$ and $St \simeq 0.15$, but without a dominating sharp peak at the lock-in frequency.

Displaying the polar plots at a later time range from Fig. 12a, where the oscillation amplitude has decayed, leads to the results in Fig. 12d: the phases of the modal forces are scattered between 35° and 120°, confirming the absence of coherent forcing. This phase

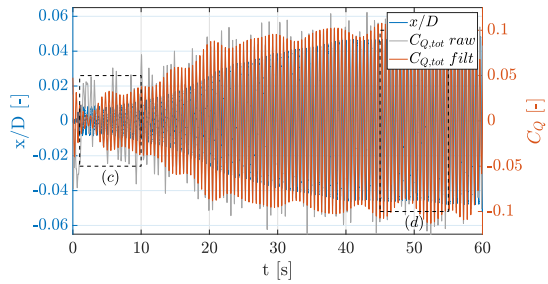

(a) Displacement and total force coefficient time history.

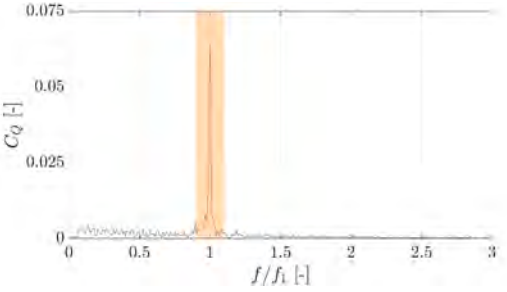

(b) Spectrum of the total force coefficient.

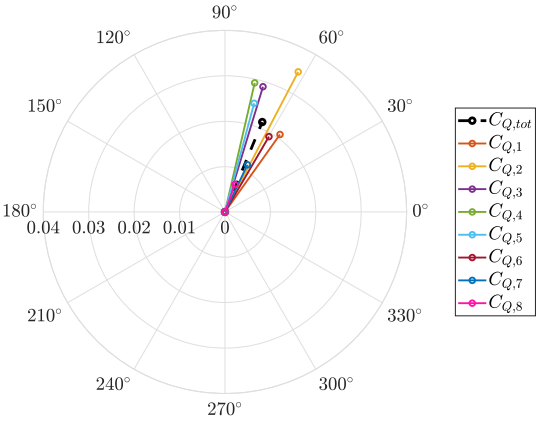

(c) Polar plot, zoom $t = [2, 12]$ s, rising VIV.

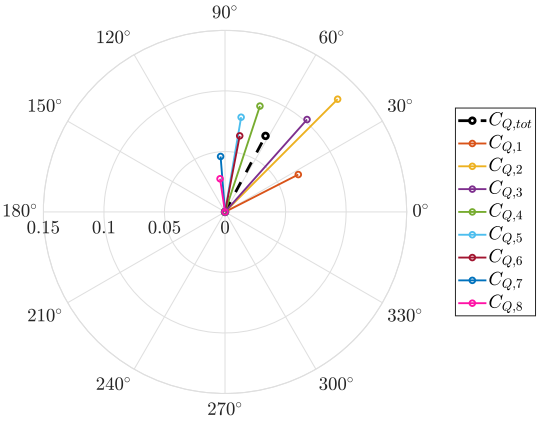

(d) Polar plot, zoom $t = [45, 55]$ s, fully developed VIV.

Fig. 13. Porous configuration, $U/U_{cr} = 0.98$, imposed initial displacement (EI).

dispersion is a quantitative indicator of the system's inability to sustain VIV. The scattered energy distribution is also visible from the Lagrangian component spectra of floors 2-3-4-5 (Fig. 14b), where no consistent peak at the lock-in frequency is found.

Given the already-observed dependency on the initial conditions in the porous configuration, it is interesting to visualize through the polar plot the effects of a finite perturbation as a trigger of the VIV.

The imposed perturbation in EI tests consists of an impulse-like initial input. A single-step transverse displacement of amplitude $x_0/D \simeq 0.1$ is applied instantaneously at the top of the building while the wind speed is in steady-state conditions at $U/U_{cr} = 0.98$. Figs. 13a–b report the time histories of structural response and total forcing and its spectrum.

During the initial cycles (Fig. 13c), the force contributions across levels become more coherent, particularly at level 2, which aligns with the total force and actively drives the oscillation. Computing the spectra of the Lagrangian components of top floors (Fig. 14c), the synchronization at the lock-in frequency is predominant, with a residual contribution at $St \simeq 0.05$ that persists but remains secondary. The force spectra confirm that all components synchronize at the lock-in frequency, while a residual contribution at $St \simeq 0.05$ persists but remains secondary.

This reveals that, in this case, the porous-induced mode is not capable of preventing VIV by itself; the role of the external input is predominant, triggering the onset of spatially coherent motion-induced forces synchronized with the structure's natural frequency.

Once VIV is established (45-55s in Fig. 13a), the phase distribution among levels resembles that of the naked configuration, with an inverse dependence on floor height. This shows that, after onset, the fluid-structure system behaves as if the shroud were absent.

These findings confirm the capability of a porous covering to alter VIV initiation by desynchronizing wind-induced forces at different levels along the height of the building, responsible for a more scattered energy distribution in the force spectrum. In build-up tests, the dominant shedding frequency is associated with the separated shear layer at the shroud edges; this low-frequency mode cannot excite the structural natural frequency, and oscillations remain suppressed. When an external perturbation is applied, however, motion-induced forces emerge at f_1, leading to synchronization and VIV development with characteristics nearly identical to those of the naked prism. Porosity, therefore, acts as a *conditional mitigation strategy*: it raises the threshold for instability and prevents spontaneous oscillations under quiescent conditions, while leaving the system susceptible to vibrations once finite disturbances are introduced.

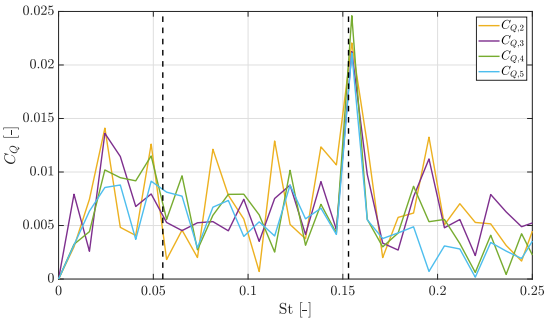

(a) BU, $t = [2, 12]s$, rising VIV.

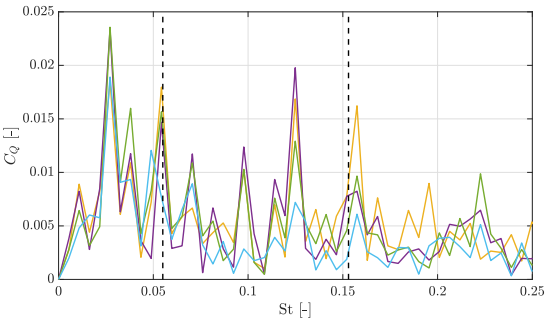

(b) BU, $t = [35, 45]s$, no VIV.

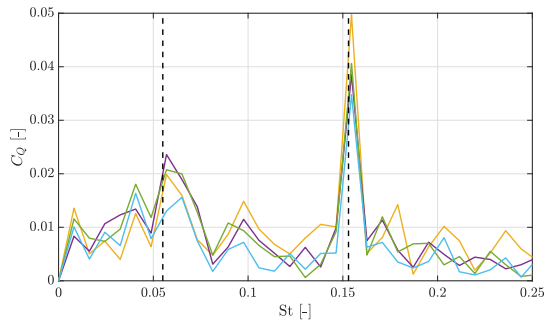

(c) EI, $t = [2, 12]s$, rising VIV.

Fig. 14. Porous configuration, $U/U_{cr} = 1.02$. Spectra of Lagrangian force components of floors 2,3,4,5. The vertical dotted black lines highlight the St number associated with porosity and motion-induced VS.

Discussion

The aeroelastic tests reveal a fundamental difference between the naked and porous configurations, which can be understood by considering the deterministic nature of vortex-induced vibrations and the effect of the porous envelope on the energy balance governing the onset of the instability.

For the naked prism, once the geometric properties, modal parameters, and inflow conditions are fixed, the VIV response is inherently deterministic. Any non-zero initial motion converges to the same limit-cycle oscillation. This behaviour is characteristic of vortex-induced vibrations (Williamson and Govardhan, 2004; Zasso et al., 2008). In the present experiments, this property is demonstrated by the correspondence between progressive-regime (PR) tests, where each operating point is reached with a finite initial displacement, and build-up (BU) tests from rest. As shown in the previous sections, both procedures lead to identical steady-state displacement, force, frequency, and phase relationships. This confirms that, in the naked configuration, vortex shedding already provides sufficient aerodynamic energy to trigger synchronization, regardless of the type or amplitude of the initial perturbation.

The porous configuration behaves fundamentally differently. The absence of oscillations in BU tests indicates that the porous envelope introduces an effective stabilizing mechanism, which may be interpreted as an aerodynamic added-damping effect. Several studies on porous coverings report similar reductions in forcing efficiency and increases in the threshold for VIV onset (Hu et al., 2017; Catania et al., 2024). In this scenario, the aerodynamic energy extracted from the flow during the early cycles is insufficient

to overcome the damping contributions of the structure and the porous layer, and the oscillations decay. An externally imposed displacement, however, provides the additional initial energy required to activate motion-induced forces, allowing the system to reach the synchronization threshold and develop VIV. This explains why the porous model oscillates in EI and PR tests but not in BU conditions.

This mechanism also clarifies why VIV may still arise at $U = 0.98\,U_{cr}$ in PR tests. At this velocity, the aerodynamic forcing is maximum, and even small naturally occurring perturbations, such as low-level buffeting, can supply sufficient energy to exceed the onset threshold. At other reduced velocities, the reduced VS energy and the stabilizing effect of the porous layer make spontaneous VIV onset unlikely, which is consistent with the observed phase behaviour of the modal forces.

These observations demonstrate that the porous façade alters the *onset* dynamics of VIV by increasing the energy threshold required to initiate lock-in, while leaving the *post-onset* limit-cycle behaviour essentially unchanged. Once synchronization occurs, the system evolves like the naked configuration, confirming that porosity acts as a conditional mitigation strategy capable of preventing self-excited oscillations under quiescent conditions but not under sufficiently energetic perturbations.

7. Conclusions

This study investigated how a porous façade modifies the aerodynamic and aeroelastic behavior of a rectangular prism with aspect ratio $B/D = 3.33$, representative of a high-rise building. A combined experimental and numerical approach was adopted, with wind tunnel tests on rigid and aeroelastic models and Wall-Modeled Large-Eddy Simulations (WMLES) using a Darcy-Forchheimer homogenized representation of porosity. Main findings can be summarized as follows:

- Rigid-model tests reveal that the pressure distribution on the building's façade is strongly affected by the presence of the porous covering. This is valid for both the mean and the oscillating part, with more uniform distributions from the porous configurations.
- The CFD simulations reproduced these features with good accuracy, validating the Darcy-Forchheimer approach as a reliable tool for capturing the global aerodynamic loads and the detailed pressure field in porous-covered configurations. Beyond rigid-body aerodynamics, the model provides physical insight into the flow mechanisms underlying the experimental observations, confirming its value as an interpretative and predictive tool.
- Making advantage of the combined experimental and CFD approaches, the rigid-model analysis showed that the porous layer significantly alters vortex shedding and the mechanism behind such modification. Additional separation points form at the windward edges of the envelope, producing shear layers that interact with those generated from the inner façade. Their coalescence widens the wake and shifts the main shedding frequency from $St = 0.14$ to $St \simeq 0.05$. The porous covering also leads to a more uniform pressure distribution on the sheltered surface, consistent with its shielding effect.
- When aeroelastic effects are considered, above a certain Scruton threshold, the porous façade modifies the initiation of VIV. In build-up tests, the coherence among modal force components in the first oscillation cycles is disrupted, preventing the lock-in process. In this regime, the force spectrum is dominated by a low-frequency contribution associated with porosity, and vibrations remain suppressed. However, when the system is perturbed by an imposed initial displacement, the force components synchronize and VIV develops with amplitudes and phase behavior similar to the naked case. This highlights the conditional nature of the mitigation: porosity raises the energy threshold required for oscillation onset, effectively preventing self-excited motion under quiescent conditions, but not when significant disturbances are present.

These findings clarify the mechanisms by which porous façades influence vortex shedding and VIV initiation. While the results demonstrate the potential of porosity as a conditional mitigation strategy, further studies are needed to extend the analysis to different porosity levels, façade configurations, and mass-damping conditions before practical design recommendations can be formulated.

Declaration of generative AI and AI-assisted technologies in the writing process

During the preparation of this work, the authors used OpenAI's ChatGPT to assist in improving the clarity, coherence, and readability of various sections of the manuscript. Specifically, the tool was employed to rephrase technical descriptions, enhance the flow of the narrative, and suggest alternative formulations for complex concepts. After using this tool, the authors carefully reviewed, validated, and edited the content to ensure technical accuracy and compliance with the research objectives. The authors take full responsibility for the content of the publication.

CRediT authorship contribution statement

Marcello Catania: Writing – review & editing, Writing – original draft, Visualization, Validation, Software, Methodology, Investigation, Formal analysis, Data curation, Conceptualization; **Giulia Pomaranzi:** Writing – review & editing, Visualization, Supervision, Investigation, Formal analysis; **Alberto Zasso:** Supervision, Funding acquisition.

Data availability

Data will be made available on request.

Further development

The findings open several directions for future work. The analysis here was limited to a single porous façade configuration; further studies should examine the influence of porosity ratio and installation distance from the inner face, as well as other façade geometries commonly used in architecture, such as louvers and patterned double-skin systems. The validated numerical framework provides a powerful tool to complement experimental work and to facilitate exploring the effectiveness of different façade configurations. The Darcy-Forchheimer model, shown to accurately reproduce the rigid behavior, can be upgraded the aeroelastic configuration to dive into the characteristics of VIV also numerically. Moreover, it could be exploited to conduct systematic parametric studies to explore not only different porosity values and façade spacings, but also the aerodynamic and aeroelastic performance of a wider range of two- and three-dimensional porous coverings. Finally, extending the analysis to different mass-damping conditions and inflow turbulence levels will help quantify the robustness and practical applicability of porous façades as a VIV mitigation strategy for civil infrastructure.

Declaration of competing interest

The authors declare that they have no known competing financial interests or personal relationships that could have appeared to influence the work reported in this paper.

References

Alqaed, S., 2022. Effect of annual solar radiation on simple façade, double-skin facade and double-skin facade filled with phase change materials for saving energy. Sustain. Energy Technol. Assess. 51, 101928. https://doi.org/10.1016/j.seta.2021.101928

Alvarez, A.J., Nieto, F., Nguyen, D.T., Owen, J.S., Hernandez, S., 2019. 3D LES simulations of a static and vertically free-to-oscillate 4:1 rectangular cylinder: effects of the grid resolution. J. Wind Eng. Ind. Aerodyn. 192, 31–44. https://doi.org/10.1016/j.jweia.2019.06.012

Ansari, H., Naeeni, S., 2024. On the influence of porous coating on vibration response and noise reduction of cylinders at high reynolds numbers. Phys. Fluids 36 (7), 075169. https://doi.org/10.1063/5.0206943

Barbosa, S., Ip, K., 2014. Perspectives of double skin façades for naturally ventilated buildings: a review. Renew. Sustain. Energy Rev. 40, 1019–1029. https://doi.org/10.1016/j.rser.2014.07.192

Bruno, L., Coste, N., Fransos, D., 2012. Simulated flow around a rectangular 5:1 cylinder: spanwise discretisation effects and emerging flow features. J. Wind Eng. Ind. Aerodyn. 104–106, 203–215. 13th International Conference on Wind Engineering. https://doi.org/10.1016/j.jweia.2012.03.018

Bruno, L., Fransos, D., Coste, N., Bosco, A., 2010. 3D flow around a rectangular cylinder: a computational study. J. Wind Eng. Ind. Aerodyn. 98 (6), 263–276. 6th International Colloquium on Bluff Body Aerodynamics and Applications. https://doi.org/10.1016/j.jweia.2009.10.005

Bruno, L., Salvetti, M.V., Ricciardelli, F., 2014. Benchmark on the aerodynamics of a rectangular 5:1 cylinder: an overview after the first four years of activity. J. Wind Eng. Ind. Aerodyn. 126, 87–106. https://doi.org/10.1016/j.jweia.2014.01.005

Cao, Y., Tamura, T., 2016. Large-eddy simulations of flow past a square cylinder using structured and unstructured grids. Comput. Fluids 137, 36–54. https://doi.org/10.1016/j.compfluid.2016.07.013

Catania, M., Pomaranzi, G., Zasso, A., 2024. The role of permeable double skin façades on the onset of VIV on high-rise buildings. J. Wind Eng. Ind. Aerodyn. 253, 105831. https://doi.org/10.1016/j.jweia.2024.105831

Chan, A.L.S., Chow, T.T., Fong, K.F., Lin, Z., 2009. Investigation on energy performance of double skin façade in hong kong. Energy Build. 41 (11), 1135–1142. https://doi.org/10.1016/j.enbuild.2009.05.012

Chen, H., Christensen, E.D., 2016. Investigations on the porous resistance coefficients for fishing net structures. J. Fluids Struct. 65, 76–107. https://doi.org/10.1016/j.jfluidstructs.2016.05.005

Deville, M.O., 2022. Boundary Layer. Springer International Publishing, Cham. 175–195. https://doi.org/10.1007/978-3-031-04683-4_7

Eissa, M., Metwally, O., Alawode, K.J., Elawady, A., Lori, G., 2025. Performance of high-rise building façades under wind loading: a state-of-the-art review. J. Build. Eng. 114072. https://doi.org/10.1016/j.jobe.2025.114072

Franco, R., Celis, C., da Silva, L.F.F., 2023. Numerical simulation of bluff body turbulent flows using hybrid RANS/LES turbulence models. J. Brazil. Soc. Mech. Sci. Eng. 45 (4), 217. https://doi.org/10.1007/s40430-023-04148-3

Georgiadis, N.J., Mankbadi, M.R., 2015. Examination of parameters affecting large-eddy simulations of flow past a square cylinder. AIAA J. 53 (6), 1706–1718. https://doi.org/10.2514/6.2014-2089

Giachetti, A., Manara, G., Bartoli, G., 2025. Permeable building envelopes: a literature review and a novel classification from the wind load perspective. J. Build. Eng. 114005. https://doi.org/10.1016/j.jobe.2025.114005

Griffin, O.M., 1978. A universal strouhal number for the 'locking-on' of vortex shedding to the vibrations of bluff cylinders. J. Fluid Mech. 85 (3), 591–606. https://doi.org/10.1017/S0022112078000804

Grozescu, A.N., Bruno, L., Fransos, D., Salvetti, M.V., 2011a. Large-eddy simulations of a benchmark on the aerodynamics of a rectangular 5:1 cylinder. In: Proceedings of the 20Th Italian Conference on Theoretical and Applied Mechanics. Bologna, Italy.

Grozescu, A.N., Salvetti, M.V., Camarri, S., Buresti, G., 2011b. Variational multiscale large-eddy simulations of the BARC flow configuration. In: Proceedings of the Thirteenth International Conference on Wind Engineering. Amsterdam, The Netherlands.

Hu, G., Hassanli, S., Kwok, K.C.S., Tse, K.T., 2017. Wind-induced responses of a tall building with a double-skin façade system. J. Wind Eng. Ind. Aerodyn. 168, 91–100. https://doi.org/10.1016/j.jweia.2017.05.008

Hu, G., Song, J., Hassanli, S., Ong, R., Kwok, K.C.S., 2019. The effects of a double-skin façade on the cladding pressure around a tall building. J. Wind Eng. Ind. Aerodyn. 191, 239–251. https://doi.org/10.1016/j.jweia.2019.06.005

Jafari, M., Alipour, A., 2021a. Aerodynamic shape optimization of rectangular and elliptical double-skin façades to mitigate wind-induced effects on tall buildings. J. Wind Eng. Ind. Aerodyn. 213, 104586. https://doi.org/10.1016/j.jweia.2021.104586

Jafari, M., Alipour, A., 2021b. Methodologies to mitigate wind-induced vibration of tall buildings: a state-of-the-art review. J. Build. Eng. 33, 101582. https://doi.org/10.1016/j.jobe.2020.101582

Jeong, J., Hussain, F., 1995. Hussain, f.: on the identification of a vortex. JFM 285, 69–94. J. Fluid Mech. 285, 69–94. https://doi.org/10.1017/S0022112095000462

Kawai, H., 1998. Effect of corner modifications on aeroelastic instabilities of tall buildings. J. Wind Eng. Ind. Aerodyn. 74–76, 719–729. https://doi.org/10.1016/S0167-6105(98)00065-8

Kawai, S., Larsson, J., 2012. Wall-modeling in large eddy simulation: length scales, grid resolution, and accuracy. Phys. Fluids 24 (1), 015105. https://doi.org/10.1063/1.3678331

Larsson, J., Kawai, S., Bodart, J., Bermejo Moreno, I., 2016. Large eddy simulation with modeled wall-stress: recent progress and future directions. Mech. Eng. Rev. 3 (1), 15–00418–15–00418. https://doi.org/10.1299/mer.15-00418

Li, M., Li, S., Liao, H., Zeng, J., Wang, Q., 2016. Spanwise correlation of aerodynamic forces on oscillating rectangular cylinder. J. Wind Eng. Ind. Aerodyn. 154, 47–57. https://doi.org/10.1016/j.jweia.2016.04.003

Marykovskiy, Y., Pomaranzi, G., Schito, P., Zasso, A., 2024. A method to evaluate forchheimer resistance coefficients for permeable screens and air louvers modelled as a porous medium. Fluids 9 (7). https://doi.org/10.3390/fluids9070147
Nakamura, Y., 1996. Vortex shedding from bluff bodies and a universal strouhal number. J. Fluids Struct. 10 (2), 159–171. https://doi.org/10.1006/jfls.1996.0011
Naudascher, E., Wang, Y., 1993. Flow-induced vibrations of prismatic bodies and grids of prisms. J. Fluids Struct. 7 (4), 341–373. https://doi.org/10.1006/jfls.1993.1021
Païdoussis, M.P., Price, S.J., de Langre, E., 2010. Vortex-Induced Vibrations. Cambridge University Press. 105–154
Pelletier, K., Wood, C., Calautit, J., Wu, Y., 2023. The viability of double-skin façade systems in the 21st century: a systematic review and meta-analysis of the nexus of factors affecting ventilation and thermal performance, and building integration. Build. Environ. 228, 109870. https://doi.org/10.1016/j.buildenv.2022.109870
Piomelli, U., 2008. Wall-layer models for large-eddy simulations. Prog. Aerosp. Sci. 44 (6), 437–446. Large Eddy Simulation - Current Capabilities and Areas of Needed Research. https://doi.org/10.1016/j.paerosci.2008.06.001
Pomaranzi, G., Bistoni, O., Schito, P., Rosa, L., Zasso, A., 2021. Wind effects on a permeable double skin façade, the ENI head office case study. Fluids 6, 415. https://doi.org/10.3390/fluids6110415
Pomaranzi, G., Daniotti, N., Schito, P., Rosa, L., Zasso, A., 2020. Experimental assessment of the effects of a porous double skin façade system on cladding loads. J. Wind Eng. Ind. Aerodyn. 196, 104019. https://doi.org/10.1016/j.jweia.2019.104019
Pomaranzi, G., Pasqualotto, G., Zasso, A., 2022. Investigation of the effects due to a permeable double skin façade on the overall aerodynamics of a high-rise building. Wind Struct. Int. J. 35 (3), 213–227. https://doi.org/10.12989/was.2022.35.3.213
Pope, S.B., 2000. Turbulent Flows. Cambridge University Press.
Ramesh, N.T., Yarusevych, S., Morton, C., 2025. Transient vortex-induced vibrations of a cylinder released from rest. J. Fluids Struct. 133, 104262. https://doi.org/10.1016/j.jfluidstructs.2024.104262
Rastan, M.R., Shahbazi, H., Sohankar, A., Alam, M.M., Zhou, Y., 2021. The wake of a wall-mounted rectangular cylinder: cross-sectional aspect ratio effect. J. Wind Eng. Ind. Aerodyn. 213, 104615. https://doi.org/10.1016/j.jweia.2021.104615
Rastan, M.R., Sohankar, A., Alam, M.M., 2017. Low-reynolds-number flow around a wall-mounted square cylinder: flow structures and onset of vortex shedding. Phys. Fluids 29 (10).
Ricci, M., Patruno, L., de Miranda, S., Ubertini, F., 2017. Flow field around a 5:1 rectangular cylinder using LES: influence of inflow turbulence conditions, spanwise domain size and their interaction. Comput. Fluids 149, 181–193. https://doi.org/10.1016/j.compfluid.2017.03.010
Rocchio, B., Mariotti, A., Salvetti, M.V., 2020. Flow around a 5:1 rectangular cylinder: effects of upstream-edge rounding. J. Wind Eng. Ind. Aerodyn. 204, 104237. https://doi.org/10.1016/j.jweia.2020.104237
Shimada, K., Ishihara, T., 2002. Application of a modified k-ϵ model to the prediction of aerodynamic characteristics of rectangular cross-section cylinders. J. Fluids Struct. 16 (4), 465–485. https://doi.org/10.1006/jfls.2001.0433
Sohankar, A., 2008. Large eddy simulation of flow past rectangular-section cylinders: side ratio effects. J. Wind Eng. Ind. Aerodyn. 96 (5), 640–655. https://doi.org/10.1016/j.jweia.2008.02.009
Sumner, D., Rostamy, N., Bergstrom, D.J., Bugg, J.D., 2017. Influence of aspect ratio on the mean flow field of a surface-mounted finite-height square prism. Int. J. Heat Fluid Flow 65, 1–20. https://doi.org/10.1016/j.ijheatfluidflow.2017.02.004
Tamura, T., Miyagi, T., Kitagishi, T., 1998. Numerical prediction of unsteady pressures on a square cylinder with various corner shapes. J. Wind Eng. Ind. Aerodyn. 74–76, 531–542. https://doi.org/10.1016/S0167-6105(98)00048-8
Teimourian, A., Teimourian, H., 2021. Vortex shedding suppression: a review on modified bluff bodies. Eng 2 (3), 325–339. https://doi.org/10.3390/eng2030021
Wang, H.F., Zhou, Y., 2009. The finite-length square cylinder near wake. J. Fluid Mech. 638, 453–490.
Wang, X., Xu, F., Zhang, Z., Wang, Y., 2024. 3D LES numerical investigation of vertical vortex-induced vibrations of a 4:1 rectangular cylinder. Adv. Wind Eng. 1 (1), 100008. https://doi.org/10.1016/j.awe.2024.100008
Wang, Y., Chen, Y., Li, C., 2020. Energy performance and applicability of naturally ventilated double skin façade with venetian blinds in yangtze river area. Sustain. Cities Soc. 61, 102348. https://doi.org/10.1016/j.scs.2020.102348
Williamson, C.H.K., Govardhan, R.N., 2004. Vortex-induced vibrations. Wind Effect. Struct. https://api.semanticscholar.org/CorpusID:58937745
Xu, M., Patruno, L., Lo, Y.-L., Miranda, S., Ubertini, F., 2022a. On the numerical simulation of perforated bluff-bodies: a CFD study on a hollow porous 5:1 rectangular cylinder. Wind Struct. Int. J. 34, 1–14. https://doi.org/10.12989/was.2022.34.1.001
Xu, M., Patruno, L., Lo, Y.-L., Miranda, S., Ubertini, F., 2022b. Simulation of porous claddings using LES and URANS: a 5:1 rectangular cylinder. Wind Struct. Int. J. 35, 67–81. https://doi.org/10.12989/was.2022.35.1.067
Yang, Q., Zheng, C., Ruan, G., Liu, X., 2025. Aerodynamic characteristics of rounded-corner rectangular cylinders based on wind tunnel model test. Exp. Therm Fluid Sci. , 111566. https://doi.org/10.1016/j.expthermflusci.2025.111566
Yuan, W., Li, J., Zhang, C., Zhang, W., Xu, H., 2021. Influence of porous media coatings on flow characteristics and vortex-induced vibration of circular cylinders. J. Fluids Struct. 106, 103365. https://doi.org/10.1016/j.jfluidstructs.2021.103365
Yu, D., Kareem, A., 1998. Parametric study of flow around rectangular prisms using LES. J. Wind Eng. Ind. Aerodyn. 77–78, 653–662. https://doi.org/10.1016/S0167-6105(98)00180-9
Zasso, A., Belloli, M., Giappino, S., Muggiasca, S., 2008. Pressure field analysis on oscillating circular cylinder. J. Fluids Struct. 24 (5), 628–650.
Zdravkovich, M.M., 1997. Flow around circular cylinders: Volume 2: Applications. Oxford university press. Vol. 2,
Zhao, M., 2023. A review of recent studies on the control of vortex-induced vibration of circular cylinders. Ocean Eng. 285, 115389. https://doi.org/10.1016/j.oceaneng.2023.115389